

Top gating of epitaxial $(\text{Bi}_{1-x}\text{Sb}_x)_2\text{Te}_3$ topological insulator thin films

Fan Yang, A. A. Taskin, Satoshi Sasaki, Kouji Segawa, Yasuhide Ohno, Kazuhiko Matsumoto, and Yoichi Ando*
Institute of Scientific and Industrial Research, Osaka University, Ibaraki, Osaka 567-0047, Japan

(Dated: May 7, 2021)

The tunability of the chemical potential for a wide range encompassing the Dirac point is important for many future devices based on topological insulators. Here we report a method to fabricate highly efficient top gates on epitaxially grown $(\text{Bi}_{1-x}\text{Sb}_x)_2\text{Te}_3$ topological insulator thin films without degrading the film quality. By combining an *in situ* deposited Al_2O_3 capping layer and a SiN_x dielectric layer deposited at low temperature, we were able to protect the films from degradation during the fabrication processes. We demonstrate that by using this top gate, the carriers in the top surface can be efficiently tuned from *n*- to *p*-type. We also show that magnetotransport properties give evidence for decoupled transport through top and bottom surfaces for the entire range of gate voltage, which is only possible in truly bulk-insulating samples.

Topological insulators (TIs) are a class of insulators possessing an energy gap in the bulk and helically spin-polarized gapless states on the surface.¹⁻³ In the last few years, great efforts and progress have been made to synthesize high-quality, bulk-insulating TI materials in various ways.⁴⁻¹³ As the materials issues being solved, the focus and interest of experimentalists start to shift to the realization of the theoretically proposed TI devices for applications ranging from spintronics to quantum computing.¹⁻³ For such devices, an efficient gate control to tune the Fermi level in a wide range is usually essential, and already many gating experiments have been done on TI materials by using different gating techniques.¹²⁻²⁰ Among the various gating techniques, top gating has an advantage to provide local control of the chemical potential, which is favorable in many applications. However, a damage-free method to fabricate efficient top gates on TIs has not yet been fully developed.

To achieve efficient top-gate controls of TI materials, there are two main difficulties. One is to obtain bulk-insulating samples, because the unwanted bulk carriers bring the Fermi level far away from the Dirac point and screen the electric field. This difficulty is being solved by means of chemical doping, in both single crystals^{4-10,12,13} and thin films.¹¹ The other difficulty is the degradations of the sample surface during the fabrication processes, especially during the deposition of the dielectric material. It has been shown that the usual methods to deposit dielectric materials such as atomic layer deposition (ALD) can cause heavy damage to the TI surface;¹⁵ such a damage would lower the surface mobility and also introduce a large number of impurity states to pin the surface chemical potential, making its gate tuning to be difficult.¹⁵ It is thus important to develop a method to fabricate top gates with minimal damage to the TI surface.

In this Letter, we report our top-gating results on $(\text{Bi}_{1-x}\text{Sb}_x)_2\text{Te}_3$ topological-insulator thin films grown by molecular beam epitaxy (MBE). Following Ref. 11, the composition of the films was optimized for achieving the bulk-insulating state. We show that a combination of an *in situ* deposited Al_2O_3 capping layer and a 200-nm-thick SiN_x dielectric layer deposited by the hot-wire chemical vapor deposition (CVD) technique at $< 80^\circ\text{C}$ makes it

possible to fabricate nearly damage-free top gate, with which an efficient ambipolar gating is possible. The mobility and carrier density of both top and bottom surfaces were estimated by fitting the magnetic-field dependences of the Hall resistivity, $R_{yx}(B)$, to the two-band model for a range of gate voltage V_g . The mobility of the top surface, $700 - 1300 \text{ cm}^2\text{V}^{-1}\text{s}^{-1}$ depending on V_g , is found to be always higher than that of the bottom surface. The weak antilocalization (WAL) effect was observed in the entire range of V_g and its analysis allows us to conclude that the top and bottom surfaces are always decoupled in our films irrespective of V_g . Our top gating technique is useful for realizing TI devices that require both the local control of the chemical potential encompassing the Dirac point *and* a high mobility of the surface state.

The $(\text{Bi}_{1-x}\text{Sb}_x)_2\text{Te}_3$ thin films were grown on sapphire (0001) substrates. In this work, the thickness was fixed at 20 nm, for which the optimized flux ratio between Bi and Sb to obtain bulk-insulating films was 0.15. After the growth, the sample was transferred to an attached electron-beam deposition chamber to deposit 4-nm-thick Al_2O_3 capping layer, during which the sample holder was cooled by running water to keep the sample temperature below 100°C . The inset of Fig. 1(b) is an atomic force microscope (AFM) image of a typical film used in this experiment, a 20-nm-thick $(\text{Bi}_{1-x}\text{Sb}_x)_2\text{Te}_3$ film capped with a 4-nm-thick Al_2O_3 capping layer. One can see atomically flat triangles with sharp edges, indicating that the Al_2O_3 layer is uniformly deposited. The step height at the edge of each triangle is about 1 nm, corresponding to the thickness of the growth unit (quintuple layer) of $(\text{Bi}_{1-x}\text{Sb}_x)_2\text{Te}_3$.

The films were fabricated into top-gated Hall-bar devices by five steps described in the following. All metal electrodes of the devices were made of 50-nm-thick Pd films deposited by magnetron sputtering.

The first step was to pattern the film into a Hall-bar shape with photolithography and wet etching. Following the wet-etching recipe for Bi_2Te_3 films,²³ we etched our $(\text{Bi}_{1-x}\text{Sb}_x)_2\text{Te}_3$ films by using the solution of 1 HCl : 0.8 H_2O_2 : 8 CH_3COOH : 16 H_2O (volume ratio); the mass concentrations of HCl, H_2O_2 , and CH_3COOH used for making this etchant were 36%, 33% and 99.7%, re-

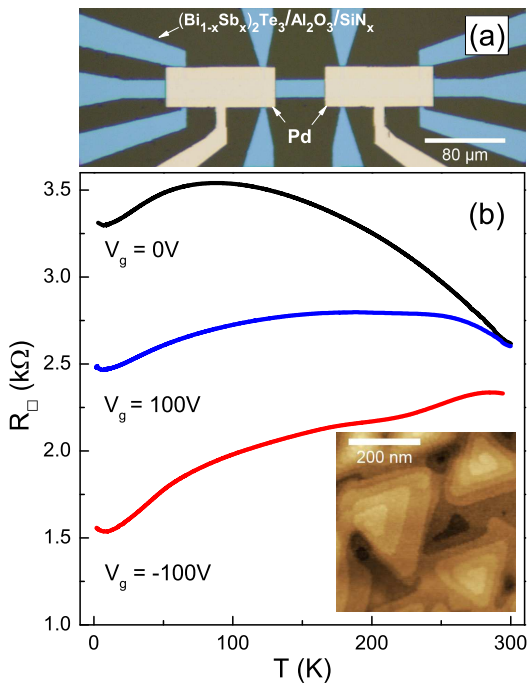


FIG. 1. (Color online) (a) Optical microscope image of the device. (b) Temperature dependences of R_{\square} , taken at $V_g = 100$ V, 0 V and -100 V. Inset: AFM image of a 20-nm-thick $(\text{Bi}_{1-x}\text{Sb}_x)_2\text{Te}_3$ film capped with 4-nm-thick Al_2O_3 .

spectively. In the second step, the resist pattern for metal contacts was defined with photolithography, and the sample was dipped into 2.4% tetramethylammonium hydroxide solution for several minutes to remove the Al_2O_3 capping layer in the contact area, followed by Pd deposition and lift-off. The third step was to deposit the dielectric layer for the top gates. A 200-nm-thick SiN_x layer was deposited by hot-wire CVD, during which the sample temperature was kept lower than 80°C ;²⁴ since there is no resist mask for this deposition, the SiN_x layer covers everywhere, including the Pd contacts on the arms of the Hall bar. The fourth step was thus to open a window in the SiN_x layer on the top of each Pd contact; this was done by photolithography and subsequent dry etching. In the final step, the top-gate electrodes were fabricated by photolithography, Pd deposition, and lift-off.

The measurements were performed in a ^4He cryostat with a base temperature of 1.8 K, by using a standard lock-in technique. The excitation current was $1 \mu\text{A}$. Using the Hall-bar-shaped samples as shown in Fig. 1(a), both the longitudinal sheet resistance R_{\square} and the Hall resistance R_{yx} were obtained by four terminal measurements, as a function of temperature T and magnetic field B . The gate voltage V_g was applied in the range of ± 100 V. When the gate voltage is cycled, we observed a hysteresis in both R_{\square} and R_{yx} ; this is probably due to impurity states that trap charges. Hence, to keep consistency in the data, all curves shown here were taken upon decreasing V_g from $+100$ V to -100 V.

Figure 1(b) shows the R_{\square} vs. T curves measured at three gate voltages. One can see that the effect of top gating on the $R_{\square}(T)$ behavior is large; in particular, R_{\square} changes by more than a factor of two at low temperature. One may notice that there is a weak upturn in all three curves at the lowest temperatures; such an upturn has been reported for TI thin films in the past,^{25–27} and is discussed to be due to electron interaction effects.^{28,29}

The $R_{yx}(B)$ curves showed significant and complicated changes when V_g is varied. In Fig. 2, to present its changes in a comprehensible manner, we divide the $R_{yx}(B)$ curves measured at various V_g values into three groups [Figs. 2(a) – 2(c)] and discuss them separately:

In the first group [Fig. 2(a)], the slopes of the curves are negative, corresponding to n -type carriers. The negative slope increases with decreasing V_g , becoming the steepest at $V_g = 26$ V. Hence, in this regime the number of mobile electrons decreases as V_g is reduced. Below $V_g = 50$ V, the $R_{yx}(B)$ curves start to show nonlinearity.

In the second group [Fig. 2(b)], while the dominant carriers are still n -type, the slope now decreases with decreasing V_g , and the $R_{yx}(B)$ curves become more nonlinear at lower V_g . This suggests that the chemical potential of the top surface is lowered sufficiently to cross the Dirac point and p -type carriers start to show up on the top surface; on the other hand, the bottom surface, which feels screened electric field and is less sensitive to V_g , still harbors n -type carriers.

In the third group [Fig. 2(c)], as V_g is lowered into large negative values, the slope of $R_{yx}(B)$ changes from negative to positive, indicating a switchover in the dominant carrier type. In this regime, the density of p -type carriers in the top surface steadily increases with decreasing V_g , causing the whole $R_{yx}(B)$ curve to show positive slope at $V_g = -100$ V.

The V_g dependences of the Hall coefficient R_H and R_{\square} are summarized in Fig. 2(d). Since the $R_{yx}(B)$ curves were nonlinear in the majority of the V_g range, we define the slopes of $R_{yx}(B)$ at $B = 0$ and 8.9 T as the R_H values at those fields. The insets in Fig. 2(d) depict the location of the chemical potential at the top and bottom surfaces for different V_g regimes. At high positive and negative gate voltages, the carrier type of the top surface is n and p , respectively. However, at $V_g = 26$ V, $|R_H|$ reaches a maximum, meaning that the number of mobile carriers becomes minimal at this V_g ; such a behavior is expected when the Fermi level of the top surface hits the Dirac point. The peak in R_{\square} is located at $V_g = 13$ V, which is a little different from the maximum position of $|R_H|$. Such a behavior is frequently reported in gating results of TIs^{16,17,20} and is likely to be due to a difference in the mobility of the carriers in the top and bottom surfaces.

The observed ambipolar gating suggests that the chemical potential in our sample is located within the bulk band gap in the majority of the V_g range, where the main contribution to the transport comes from the two surfaces channels. Therefore, one would expect that the two-band model³ to consider two independent surface

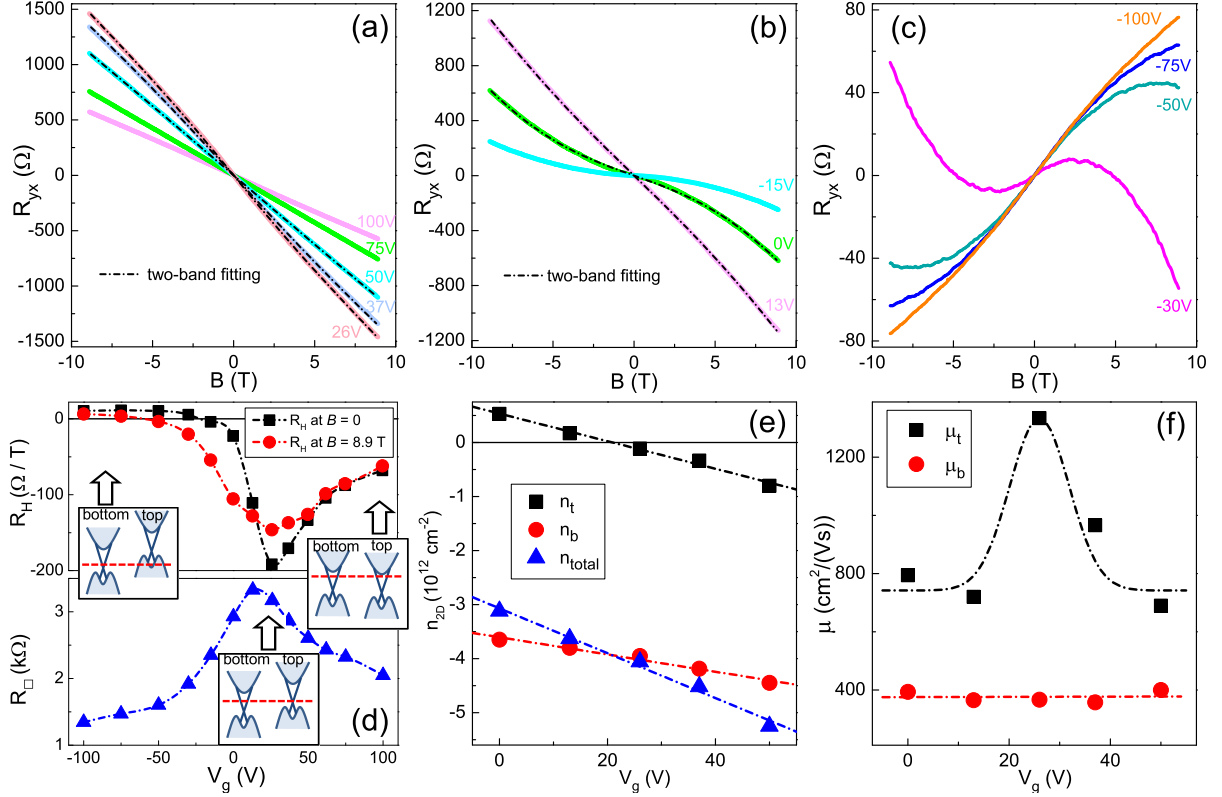


FIG. 2. (Color online) (a)-(c) R_{yx} vs. B data at different V_g values. The dashed-dotted lines in (a) and (b) show fittings to the two-band model. (d) V_g dependence of R_H (upper panel) and R_{\square} (lower panel). The insets are schematic band diagrams for three characteristic regimes. (e) Sheet carrier density vs. V_g for the top (n_t) and bottom (n_b) channels, as well as their sum (n_{total}). (f) Mobility vs. V_g for top and bottom surfaces. The data in (e) and (f) are the results of the two-band analysis.

channels would describe the $R_{yx}(B)$ behavior. Indeed, as we show below, for the V_g range of 0 – 50 V, the fitting of the $R_{yx}(B)$ data to the two-band model gives reasonable and consistent parameters for the two surfaces, which reconfirms that it is not necessary to consider an additional bulk channel. It should be noted, however, that at large positive V_g values, the $R_{yx}(B)$ curves becomes essentially linear and featureless, which prohibits us from extracting reliable information from the two-band analysis. Also, since the top of the bulk valence band is located close to the Dirac point,¹¹ at negative V_g values the Fermi level at the top surface is brought into the bulk valence band, causing the top surface to harbor conventional inversion layer (topologically trivial two-dimensional states with p -type carriers) alongside the p -type Dirac fermions; this causes the transport to occur through three channels, and one should not apply the two-band analysis for $V_g \lesssim 0$.

In the two-band model,³ the composite Hall resistivity is given as

$$R_{yx}(B) = \left(\frac{B}{e}\right) \frac{(n_t \mu_t^2 + n_b \mu_b^2) + B^2 \mu_t^2 \mu_b^2 (n_t + n_b)}{(n_t \mu_t + n_b \mu_b)^2 + B^2 \mu_t^2 \mu_b^2 (n_t + n_b)}, \quad (1)$$

where n_t , n_b , μ_t , μ_b correspond to the sheet carrier densities and mobilities of the top and bottom surfaces. Al-

though there are four fitting parameters, one can put a constraint that the observed zero-field sheet resistance $R_{\square}|_{B=0}$ must be consistent with $1/(en_t \mu_t + en_b \mu_b)$, which reduces the number of free parameters to three.³

The fittings of the data for $V_g = 0 - 50$ V to Eq. (1) are shown in Figs. 2(a) and 2(b), and the obtained parameters are shown in Figs. 2(e) and 2(f). One can see that both n_t and n_b present linear V_g dependences, and the slope is larger for $n_t(V_g)$ (i.e., the top surface is more efficiently gated), which is reasonable and reassures our assumption of two transport channels. The sign change in n_t at $V_g \approx 26$ V indicates that the Fermi level of the top surface hits the Dirac point at this V_g .

In Fig. 2(f), one can see that μ_t presents a peak value of 1300 cm 2 V $^{-1}$ s $^{-1}$ near the Dirac point, and elsewhere μ_t remains around 750 cm 2 V $^{-1}$ s $^{-1}$. Such an enhancement of the mobility near the Dirac point is often observed in graphene and is due to the vanishing of the phase space available for scattering.^{30,31} One may also notice that the bottom-surface mobility $\mu_b \simeq 375$ cm 2 V $^{-1}$ s $^{-1}$ is much lower than μ_t , meaning that the electron scattering is stronger at the interface with sapphire substrate than at the interface with Al $_2$ O $_3$ capping layer. We have also measured the $R_{yx}(B)$ curves in capping-layer free (Bi $_{1-x}$ Sb $_x$) $_2$ Te $_3$ films without any patterning

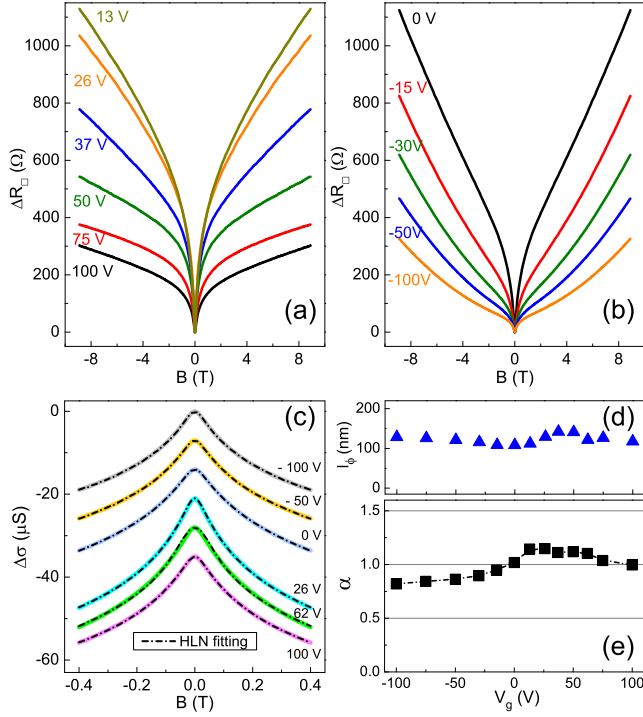


FIG. 3. (Color online) (a)-(b) Magnetoresistance at different gate voltages; (a) is for $V_g \geq 13$ V and (b) is for $V_g \leq 0$ V. (c) Magnetoconductance at representative V_g values; the curves are shifted vertically for clarity. The dashed-dotted lines are the fittings to Eq. (2). (d)-(e) V_g dependences of (d) l_ϕ and (e) α obtained from the fittings.

nor gate fabrication, and in such pristine films, μ_t was found to be typically $\sim 800 \text{ cm}^2 \text{V}^{-1} \text{s}^{-1}$. This indicates that the Al_2O_3 capping layer is indeed effective in keeping the top-surface mobility from degradation. In passing, we observed that the capping layer tends to dope p -type carriers to the surface, causing the top surface band to be slightly bent up.

Now we discuss the WAL effect in our films to see if the top and bottom surfaces are decoupled. In Figs. 3(a) and 3(b), we plot the magnetoresistance $\Delta R_\square(B)$ [$\equiv R_\square(B) - R_\square|_{B=0}$] for various V_g values, and the curves are divided into two groups. In the first group [Fig. 3(a)], the magnetoresistance presents negative curvature throughout the magnetic-field range, while in the second group [Fig. 3(b)] the magnetoresistance seems to contain a parabolic background. Since the boundary between the two groups is $V_g = 13$ V where R_\square reaches the maximum, the change in the background in the magnetoresistance appears to be correlated with the change in the carrier type. However, the origin of this intriguing behavior is not known at the moment.

Despite the change in the high-magnetic-field background, the cusp structure in the low-magnetic-field part

of $R_\square(B)$ can always be reliably analyzed as the WAL behavior. The WAL in TIs has been intensively studied both theoretically^{32,33} and experimentally^{16,17,21,22,34-36}. The peculiar magnetic-field dependence of the electrical conductivity σ associated with WAL is described by the simplified Hikami-Larkin-Nagaoka (HLN) formula

$$\Delta\sigma(B) = -\alpha \frac{e^2}{\pi h} \left[\Psi \left(\frac{1}{2} + \frac{\hbar}{4el_\phi^2 B} \right) - \ln \left(\frac{\hbar}{4el_\phi^2 B} \right) \right], \quad (2)$$

where $\Psi(x)$ is the digamma function and l_ϕ is the phase coherence length. The parameter α is presumably 0.5 when there is only one transport channel, and it is doubled when there are two channels. We have calculated $\sigma(B)$ from the data of $R_\square(B)$ and $R_{yx}(B)$ to do the proper matrix inversion.

As shown in Fig. 3(c) for representative V_g values, all the $\Delta\sigma(B)$ curves are well fitted with the HLN formula. The parameters extracted from the fittings are plotted in Figs. 3(d) and 3(e). The l_ϕ value [Fig. 3(d)] is essentially independent of V_g , and its average value of ~ 120 nm is much larger than the film thickness. More importantly, the α value [Fig. 3(e)] is found to be close to 1 throughout our V_g range,³⁷ pointing to the existence of two independent channels that are presumably the top and bottom surfaces. It has been elucidated that in TI thin films, residual bulk carriers couple the top and bottom surfaces through the bulk to produce a single diffusive transport channel for the WAL effect, which results in the α value of 0.5.^{14,16,17,35} The α value close to 1 has been observed only in two situations: (i) a depletion layer is formed in the film due to a strong band bending at high gate voltages to electrically isolate the gated surface,^{16,17} or (ii) films are relatively thick (which avoids the hybridization of the top and bottom surface states) and bulk carriers are negligible.³⁵ In this regard, the α value in our film is nearly independent of V_g , which rules out the former possibility and points to the latter. Thus, the analysis of the WAL behavior corroborates the conclusion that our films are truly bulk-insulating.

In summary, we developed a damage-free method to fabricate efficient top gates on $(\text{Bi}_{1-x}\text{Sb}_x)_2\text{Te}_3$ topological-insulator thin films. The carrier type in the top surface can be tuned from n to p , and their mobility reaches $1300 \text{ cm}^2 \text{V}^{-1} \text{s}^{-1}$ near the Dirac point. The magnetotransport properties give evidence that our films are bulk insulating with decoupled top and bottom surfaces. The top gating method developed here would be useful for the realization of future devices based on TIs.

We acknowledge M. Kishi for technical assistance and Nanotechnology Open Facilities in Osaka University for nano-fabrication facilities. This work was supported by JSPS (KAKENHI 24740237, 24540320, 25400328, and 25220708), MEXT (Innovative Area “Topological Quantum Phenomena” KAKENHI), and AFOSR (AOARD 124038).

- * Electronic mail: y_ando@sanken.osaka-u.ac.jp
- ¹ M. Z. Hasan and C. L. Kane, *Rev. Mod. Phys.* **82**, 3045 (2010).
 - ² X. L. Qi and S. C. Zhang, *Rev. Mod. Phys.* **83**, 1057 (2011).
 - ³ Y. Ando, *J. Phys. Soc. Jpn.* **82**, 102001 (2013).
 - ⁴ Y. L. Chen, J. G. Analytis, J. H. Chu, Z. K. Liu, S. K. Mo, X. L. Qi, H. J. Zhang, D. H. Lu, X. Dai, Z. Fang, S. C. Zhang, I. R. Fisher, Z. Hussain, and Z. X. Shen, *Science* **325**, 178 (2009).
 - ⁵ D. Hsieh, Y. Xia, D. Qian, L. Wray, J. H. Dil, F. Meier, J. Osterwalder, L. Patthey, J. G. Checkelsky, N. P. Ong, A. V. Fedorov, H. Lin, A. Bansil, D. Grauer, Y. S. Hor, R. J. Cava, and M. Z. Hasan, *Nature (London)* **460**, 1101 (2009).
 - ⁶ Z. Ren, A. A. Taskin, S. Sasaki, K. Segawa, and Y. Ando, *Phys. Rev. B* **82**, 241306 (2010).
 - ⁷ Z. Ren, A. A. Taskin, S. Sasaki, K. Segawa, and Y. Ando, *Phys. Rev. B* **84**, 165311 (2011).
 - ⁸ A. A. Taskin, Z. Ren, S. Sasaki, K. Segawa, and Y. Ando, *Phys. Rev. Lett.* **107**, 016801 (2011).
 - ⁹ Z. Ren, A. A. Taskin, S. Sasaki, K. Segawa, and Y. Ando, *Phys. Rev. B* **85**, 155301 (2012).
 - ¹⁰ S. S. Hong, J. J. Cha, D. Kong, and Y. Cui, *Nat. Commun.* **3**, 757 (2012).
 - ¹¹ J. S. Zhang, C. Z. Chang, Z. C. Zhang, J. Wen, X. Feng, K. Li, M. H. Liu, K. He, L. L. Wang, X. Chen, Q. K. Xue, X. C. Ma and Y. Y. Wang, *Nat. Commun.* **2**, 574 (2011).
 - ¹² J. G. Checkelsky, Y. S. Hor, R. J. Cava, and N. P. Ong, *Phys. Rev. Lett.* **106**, 196801 (2011).
 - ¹³ D. Kong, Y. Chen, J. J. Cha, Q. Zhang, J. G. Analytis, K. Lai, Z. Liu, S. S. Hong, K. J. Koski, S.-K. Mo, Z. Hussain, I. R. Fisher, Z. X. Shen, and Y. Cui, *Nature Nanotechnol.* **6**, 705 (2011).
 - ¹⁴ J. Chen, H.J. Qin, F. Yang, J. Liu, T. Guan, F.M. Qu, G.H. Zhang, J. R. Shi, X. C. Xie, C. L. Yang, K. H. Wu, Y. Q. Li, and L. Lu, *Phys. Rev. Lett.* **105**, 176602 (2010).
 - ¹⁵ H. Liu and P. D. Ye, *Appl. Phys. Lett.* **99**, 052108 (2011).
 - ¹⁶ J. Chen, X. Y. He, K. H. Wu, Z. Q. Ji, L. Lu, J. R. Shi, J. H. Smet, and Y. Q. Li, *Phys. Rev. B* **83**, 241304 (2011).
 - ¹⁷ H. Steinberg, J. B. Laloë, V. Fatemi, J. S. Moodera, and P. Jarillo-Herrero, *Physical Review B* **84**, 233101 (2011).
 - ¹⁸ M. R. Lang, L. He, F. X. Xiu, X. X. Yu, J. S. Tang, Y. Wang, X. F. Kou, W. J. Jiang, A. V. Fedorov, and K. L. Wang, *ACS nano* (6), 295 (2011).
 - ¹⁹ D. Kim, S. Cho, N. P. Butch, P. Syers, K. Kirshenbaum, S. Adam, J. Paglione, and M. S. Fuhrer, *Nat. Phys.* **8**, 460 (2012).
 - ²⁰ X. Y. He, T. Guan, X. X. Wang, B. J. Feng, P. Cheng, L. Chen, Y. Q. Li, and K. H. Wu, *Appl. Phys. Lett.* **101**, (2012).
 - ²¹ J. Lee, J. Park, J. H. Lee, J. S. Kim, and H. J. Lee, *Phys. Rev. B* **86**, 245321 (2012).
 - ²² B. Xia, P. Ren, A. Sulaev, P. Liu, S. Q. Shen, and L. Wang, *Phys. Rev. B* **87**, 085442 (2013).
 - ²³ T. Ngai and U. Ghoshal, presented at the International Conference on Thermoelectrics, 2007 (unpublished).
 - ²⁴ K. Maehashi, Y. Ohno, K. Inoue, K. Matsumoto, T. Niki and H. Matsumura, *Appl. Phys. Lett.* **92**, 183111 (2008).
 - ²⁵ M. H. Liu, C. Z. Chang, Z. C. Zhang, Y. Zhang, W. Ruan, K. He, L. L. Wang, X. Chen, J. F. Jia, S. C. Zhang, Q. K. Xue, X. C. Ma, and Y. Y. Wang, *Phys. Rev. B* **83**, 165440 (2011).
 - ²⁶ J. Wang, A. M. DaSilva, C. Z. Chang, K. He, J. K. Jain, N. Samarth, X. C. Ma, Q. K. Xue, and M. H. W. Chan, *Phys. Rev. B* **83**, 245438 (2011).
 - ²⁷ Y. Takagaki, B. Jenichen, U. Jahn, M. Ramsteiner, and K. J. Friedland, *Phys. Rev. B* **85**, 115314 (2012).
 - ²⁸ H. K. Pal, V. I. Yudson, and D. L. Maslov, *Phys. Rev. B* **85**, 085439 (2012).
 - ²⁹ E. J. König, P. M. Ostrovsky, I. V. Protopopov, I. V. Gornyi, I. S. Burmistrov, and A. D. Mirlin, *Phys. Rev. B* **88**, 035106 (2013).
 - ³⁰ Y. B. Zhang, Y. W. Tan, H. L. Stormer, and P. Kim, *Nature* **438**, 201 (2005).
 - ³¹ K. I. Bolotin, K. J. Sikes, Z. Jiang, M. Klima, G. Fudenberg, J. Hone, P. Kim, and H. L. Stormer, *Solid State Commun.* **146**, 351 (2008).
 - ³² H. Z. Lu and S. Q. Shen, *Phys. Rev. B* **84**, 125138 (2011).
 - ³³ I. Garate and L. Glazman, *Phys. Rev. B* **86**, 035422 (2012).
 - ³⁴ H. T. He, G. Wang, T. Zhang, I. K. Sou, G. K. L. Wong, J. N. Wang, H. Z. Lu, S. Q. Shen, and F. C. Zhang, *Phys. Rev. Lett.* **106**, 166805 (2011).
 - ³⁵ D. Kim, P. Syers, N. P. Butch, J. Paglione, and M. S. Fuhrer, *Nat. Commun.* **4**, 2040 (2013).
 - ³⁶ L. Zhang, M. Dolev, Q. I. Yang, R. H. Hammond, B. Zhou, A. Palevski, Y. L. Chen, and A. Kapitulnik, *Phys. Rev. B* **88**, 121103 (2013).
 - ³⁷ Following Ref. 26, one can estimate the possible impact of the electron interaction effects on the WAL analysis; in our case, the screening parameter \tilde{F}_σ estimated from the $\sigma(T)$ behavior is only ~ 0.1 , introducing an error in α of only up to 10%.